Multiple Magnetic Mode-Based Fano Resonance in Split-Ring Resonator/Disk Nanocavities

Qing Zhang,[†,⊥] Xinglin Wen,[†,⊥] Guangyuan Li,[†] Qifeng Ruan,[‡] Jianfang Wang,[‡] and Qihua Xiong[†,§,*]

[†]Division of Physics and Applied Physics, School of Physical and Mathematical Sciences, Nanyang Technological University, Singapore 637371, [‡]Department of Physics, The Chinese University of Hong Kong, Hong Kong SAR 999077, China, and [§]NOVITAS, Nanoelectronics Centre of Excellence, School of Electrical and Electronic Engineering, Nanyang Technological University, Singapore 639798. [⊥]Q. Zhang and X. Wen contributed to this work equally.

ABSTRACT Plasmonic Fano resonance, enabled by the weak interaction between a bright super-radiant and a subradiant resonance mode, not only is fundamentally interesting, but also exhibits potential applications ranging from extraordinary optical transmission to biosensing. Here, we demonstrate strong Fano resonances in split-ring resonators/disk (SRR/D) nanocavities. The high-order magnetic modes are observed in SRRs by polarization-resolved transmission spectroscopy. When a disk is centered within the SRRs, multiple high-order magnetic modes are coupled to a broad electric dipole mode of SRR/D, leading to significant Fano resonance spectral features in near-IR regime. The strength and line shape of the Fano resonances are tuned through varying the SRR split-angle and interparticle distance between SRR and disk. Finite-difference-time-domain (FDTD) simulations are conducted to understand the coupling mechanism, and the results show good agreement with experimental data. Furthermore, the coupled structure gives a sensitivity of ~282 nm/RIU with a figure of merit ~4.

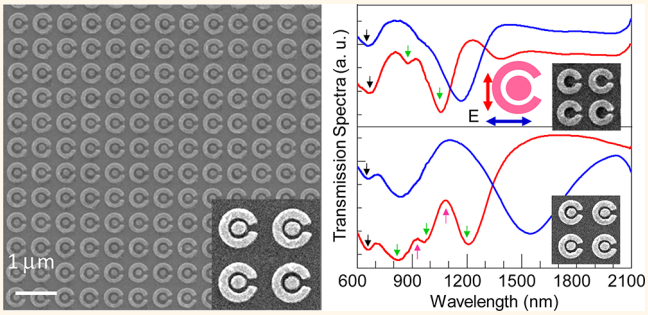

KEYWORDS: surface plasmon · Fano resonance · split-ring-resonance · magnetic mode · biosensing · surface-enhanced Raman spectroscopy

Surface plasmon has attracted great interest over the past 10 years due to its capability of manipulating light-matter interaction in nanoscale regime.[1,2] Surface plasmons bridge the gap between photons and electrons and offer opportunity to build subwavelength integrated photonic devices for quantum communication and processing.[1−3] The surface plasmon resonance (SPR) frequency is highly dependent on the geometry of metal structures and their dielectric environment, which can be utilized for numerous applications such as multicolor display/imaging and bio/chemical sensors.[2,4−6] SPR enhances the efficiency of a variety of linear and nonlinear optical processes and is beneficial for many fascinating phenomena, such as solar energy harvesting and chemical reactions.[6−11] The precise control over the optical response of plasmonic structures, especially the line shape, is essential for the practical applications.[4,12−15] For instance, SPR mode with sharp spectra feature is advantageous for chemical/biosensing, while solar cell's efficiency is benefited more from a broad absorption band.[1,7,12] In coupled plasmonic systems, which consist of several metal nanostructures with small separations, both the SPR frequency and line shape can be tailored through varying the separation and geometry.[2,3,16,17]

Fano resonance describes the interference effect between a discrete energy level and a continuum state, which produces a characteristic asymmetric line shape spectrally.[15,16,18] Plasmonic Fano resonance, occurring when a dark subradiant mode (narrow) is weakly coupled to a bright super-radiant plasmonic mode (broad), has emerged as a new method to control plasmon mode interaction and promises for applications from narrowband filter, photoswitching to high-sensitivity chem/biodetection.[4,6,12,13,17,19−23] Plasmonic Fano resonance has been demonstrated in top-down and bottom-up fabricated metallic nanodisk clusters,[24−28] and nonconcentric

* Address correspondence to qihua@ntu.edu.sg.

Received for review September 11, 2013 and accepted November 11, 2013.

Published online November 11, 2013
10.1021/nn4047716

disk/ring cavities.[13,17,21,29−31] In nanodisk clusters, the super-radiant and subradiant modes, because of the fundamental dipoles coupling in/out of phase, couple with each other *via* Fano effect. In disk/ring cavities, dark multipoles are excited by symmetry breaking and couple to the fundamental dipole modes. Recently, sharp Fano resonance asymmetric peak with a width of ~10 nm was reported as a result of the coupling between localized and waveguiding surface plasmons in Au disk/films.[19,32] Additionally, the Fano interaction between multipoles in Au nanorods was enabled by strong image charge induced by high-refractive index substrate.[33]

Besides the Fano interferences arising from pure electric field, considerable attention has been shifted to the study of Fano resonance between electric and magnetic resonance recently.[34] Theoretically, Fano-like interference between electric and magnetic resonances has been proposed in symmetry-broken looped nanoparticle trimer, where magnetic response is supported through resonant circulating displacement current.[25] Experimentally, pronounced magnetic mode-based Fano resonance was observed in asymmetric four-particle structures recently.[35] In the looped nanocluster arrays, electromagnetic near-field coupling between high-order and dipole electric modes is also possible, with regard to various experimental observations of electric Fano-resonance in planar nanoclusters.[13,24,29,36] The pure-electric and magnetic-based Fano effects may influence or even compete with each other. Split-ring-resonator (SRR) is a structure widely used as artificial metamaterials with novel electromagnetic properties such as negative magnetic permeability and negative refractive index. Although there have been a few reports on electric-mode-based Fano resonance due to the coupling between individual disks or nonconcentric ring and disk, the Fano resonance between concentric SRR and disk based upon magnetic mode has not been well understood. The SRR is selected for three reasons. First, when the ring symmetry of SRR is broken, the high-order electric modes of ring can be optically excited. Second, the high-order magnetic and electric modes of SRR can be tuned over a wide range and spectrally overlapped with super-radiant dipole modes. Third, in principle SRRs can create strong magnetic response compared with nanoparticle clusters.

In this letter, we study the plasmonic coupling in SRR/D nanocavities and focus on the interplay between the electric and magnetic mode-based Fano effects. Uniform array of gold (Au) *C*-shaped SRR concentric with disk is fabricated using electron-beam-lithography (EBL). Polarization-resolved transmission/scattering spectroscopy and finite-difference time-domain (FDTD) simulations are performed to understand the mode interactions in the SRR/D nanocavities. Multiple Fano resonances are observed as a result of the interference between a spectrally overlapping broad super-radiant dipole mode of SRR/D and high-order magnetic modes of SRR. The disk size and split angle of SRRs are varied to tune the line shape of Fano resonance. Furthermore, we show the potential applications of SRR/disk structure in refractive index sensing.

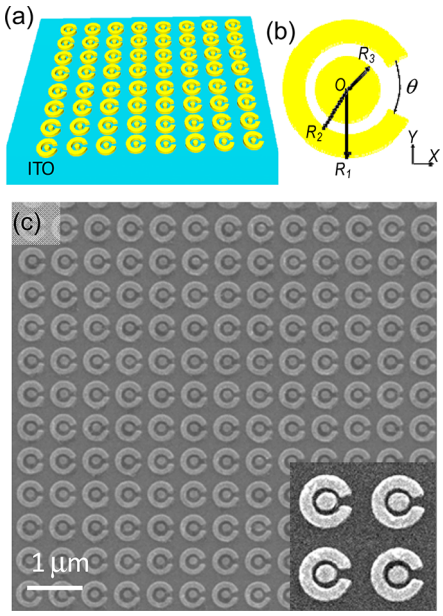

Figure 1. (a,b) Schematic of *C*-shaped split-ring resonator/disk nanocavities fabricated on ITO glass. (c) Scanning electron microscopy image of split-ring resonator/disk nanocavities arrays. The thickness is 30 nm. R_1 = 200 nm, R_2 = 110 nm, R_3 = 75 nm. θ = 15°. The separation between two units is ~150 nm.

RESULTS AND DISCUSSION

Disk, SRR, and SRR/D arrays with area of ~50 μm × 50 μm are fabricated on indium tin oxide (ITO) glass using EBL (Figure 1a), which has been presented in our previous work in detail.[37−39] Figure 1b shows the schematic structure of SRR/D nanocavity. The outer (R_1) and inner (R_2) radius of split ring is 200 and 110 nm, respectively. The radius of inner disk (R_3) is varied from 65 to 80 nm. The split angles are θ = 15°, 30°, 60°, 90°, 120°. To focus on the optical properties of individual SRR/D, the interparticle separation of two SRR/D units is set to be as large as ~150 nm to avoid the near-field coupling. The separation was varied from 150 to 750 nm, but there was no difference of transmission spectra features (Supporting Information S1), suggesting the weak near-field coupling between the adjacent SRR/D units. Figure 1c shows a representative scanning electron microscopy (SEM) image of fabricated SRR/D nanoarray, with dimensions of R_1 = 200 nm, R_2 = 110 nm, R_3 = 75 nm, θ = 15°. It can be seen that the shape and size of each SRR/D in the array are uniform. The magnified SEM image (inset) shows that the surface of as-fabricated structure is clean and flat.

Figure 2a shows the experimental transmission spectra of as-fabricated disk (Figure 2a-1), SRR (Figure 2a-2), and SRR/D (Figure 2a-3). The outer and inner radius of

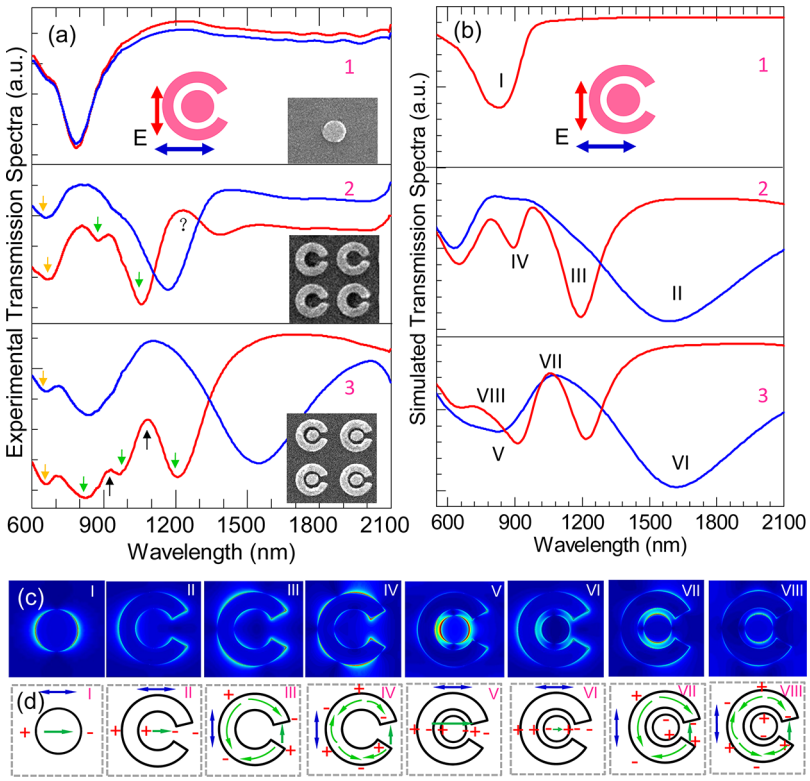

Figure 2. (a,b) Experimental (a) and calculated (b) transmission spectra of disk (1), SRR (2), and SRR/D (3) arrays. The SEM image of disk, ring, and SRR/D is included in each panel, correspondingly. The blue and red curves are transmission spectra when electric field is perpendicular and parallel to the split gap of SRR, as inset indicated. The surface plasmon resonance modes are numbered using I−VIII. (c,d) FDTD-simulated surface electric-field magnitude distribution (c) and schematic surface electric field direction and charge distribution of the surface plasmon resonance modes (d) in disk, SRR, and SRR/D. I: dipole of disk; II: dipole of SRR; III: quadrupole magnetic mode of SRR; IV: octupole magnetic mode of SRR; V: super-radiant dipole mode of SRR/D; VI: subradiant dipole modes of SRR/D; VII: Fano resonance between III and V in SRR/D; VIII: Fano resonance between IV and V in SRR/D. The blue doubled arrows show the incident electric field direction. The green arrows indicate the electric field directions.

SRR is 200 and 110 nm respectively, the disk radius is 75 nm, and the thickness is 30 nm. The blue and red curves display the spectra as the polarization is perpendicular and parallel to the split gap of SRR, respectively. The electric field direction is indicated in the inset. The scattering spectra in the range of 500−900 nm are similar to transmission spectra (Supporting Information S2).[33] Individual disk exhibits a dipole resonance dip at 787 nm irrespective of the incidence polarization direction (Figure 2a-1). The mode shows slight red-shift from 713 to 787 nm as R_3 varies from 65 to 75 nm because of the increasing aspect ratio (Supporting Information Figure S3).[16,17] On the contrary, the transmission spectra of SRR are different in the two polarization directions (Figure 2a-2). Two relatively narrow dips around 871 and 1060 nm, indicated by green arrows, can be resolved as the polarization is parallel to the split gap (red curve, Figure 2a-2). When the electric field is perpendicular to the gap, only one broad dip around 1170 nm (blue curve, Figure 2a-2) is observed. The polarization-dependent transmission spectra, thus surface plasmon resonance modes, are associated with the ring symmetry. Previous experimental and theoretical investigations on Fano resonance of individual full ring have shown that the high-order surface plasmon resonance modes (*i.e.*, quadrupole and octupole) can be optically excited besides the bright dipole modes when the ring symmetry is broken, such as side illumination.[21,29,30] In our case, when the electric field direction is parallel to split gap, the ring symmetry is broken, giving rising to the excitation of the dark high-order electron oscillation modes due to the retardation effects,[3] while when the polarization is perpendicular to the split gap, the ring symmetry is kept; therefore, only dipole-like resonance is observed. Therefore, we tentatively assign the two narrow dips located 871 and 1060 nm to the excitation of high-order surface plasmon resonance modes of the SRR. Besides, the SRR transmission spectra of both polarizations exhibit a dip located at 667 nm, indicated by orange yellow arrows in Figure 2a-2, which is corresponding to a dipole mode along the arm width of the ring.[40] The peak position does not shift with the split angle variation (shown later), supporting our assignment.

As a disk is introduced into the center of the SRR, the surface plasmon resonance modes of the SRR are coupled with the dipole mode of the disk through capacitive interaction.[1,5] When the electric field is perpendicular to the split gap, the hybridization of fundamental dipole

modes of ring and disk results in two broad dips at 834 and 1546 nm, as the blue curve in Figure 2a-3 shows. The similar results were also observed in previous reports on surface plasmon coupling of ring/disk structures, in which the two resonance modes are attributed to the antibonding and bonding coupling of the two fundamental dipole modes.[16,29,30,41] When the polarization is parallel to the split gap, the narrow modes of SRR at 871 and 1060 nm (red curve, Figure 2a-2) are overlapped with a broader dipole mode of SRR/D (834 nm) in energy. The narrow high-order resonance modes of SRR may interfere with the broad coupled dipole mode of SRR/D *via* Fano effect, leading to rich features between 700 to 1300 nm (red curve, Figure 2a-3). Particularly, the narrow mode located 871 nm is extensively overlapped with the dipole mode, leading to an evident enhanced transmission peak at 916 nm (indicated by black arrow) inside the dipole resonance absorption dip ($\sim$ 834 nm, indicated by green arrow).

Three dimensional finite-different-time-domain (FDTD) simulations of the transmission spectra and the surface electric-field magnitude distribution are performed using commercial software (Lumerical Solution, Inc.), in order to understand the plasmon interaction in SRR/D systems. The gold dielectric constant is taken from the bulk value measured by Johnson and Christy.[42] Periodic boundary condition is adopted to match the real array structures. The air environment (refractive index $n = 1$) and ITO glass substrate ($n = 1.54$) are included in the simulations. According to transmission optical setup in our measurement, a plane wave with linear polarization is used as a transmission light source. The electric-field magnitude distributions are simulated at the middle cross section of the Au structures.

Figure 2b shows the simulated transmission spectra of disk (2b-1), SRR (2b-2), and SRR/D (2b-3), respectively. The blue and red curves display the spectra when the electric field is vertical and parallel to split gap, respectively, in accordance with experimental notation in Figure 2a. The involved characteristic surface plasmon resonance modes are marked using numbers from I, II, ..., to VIII. The respective surface electric-field magnitude distributions of each surface plasmon resonance modes for a disk, a SRR, and a coupled SRR/D are presented in Figure 2c. The schematic of surface charge distribution and electric oscillation direction of the resonance modes are shown in Figure 2d accordingly. The transmission spectra show good agreement with experimental data, particularly in terms of qualitative assignment of the modes. The resonance wavelength difference between experiment and simulation may be due to the following: (1) Gold bulk dielectric constant is used in simulations, while in experiment the films are usually amorphous. (2) The dimensions of fabricated structures are slightly different from designed. Besides, the actual surface roughness structures are not captured in simulations; thus, the simulated resonance peaks are sharper than experimental data. The surface plasmon resonance of individual disk is dominated by a dipole oscillation along the disk surface (Figure 2b-1, mode I, 834 nm), clearly seen in the electric-field magnitude and charge distribution in Figure 2c,d, which is in good agreement with experimental spectra (Figure 2a-1). SRR exhibits a broad resonance when the electric field is vertical to the split gap (Figure 2b-2, blue curve, mode II), corresponding to the ring dipole mode with a symmetric bonding of two SRR arms (Figure 2c,d, mode II). The two narrow dips of SRR located at 1193 and 892 nm (Figure 2b-2, red curve, mode III and IV), resolved when the polarization is parallel to the split gap, are assigned to high-order magnetic modes of SRR. The surface electric-field magnitude distributions and direction of SRR resonance modes (Figure 2c,d, mode III and IV) confirm the excitation of quadrupole (mode III) and octupole (mode IV) along the SRR surface.[29] The circulating current (indicated by allows in Figure 2d) along the SRR can generate magnetic-dipole moment perpendicular to the SRR plane; therefore, the corresponding modes are high-order magnetic modes.[35,40] The wavelength of first-order magnetic mode whose circulating current is along the whole SRR in one direction is simulated to be around 3000 nm, which is out of our measurement spectra range. It should be noted that in the parallel polarization the experimental data show three dips, while there are just two dips in simulation. The experimental dip located at 1384 nm exhibits an evidently asymmetric line shape, which suggests a possible Fano interference between the unknown mode and magnetic quadrupole mode.

In SRR/D, when the electric field is perpendicular to the split gap, the parallel and antiparallel coupling of ring and disk dipoles gives rise to a super-radiant (Figure 2a,b-3, blue curves, mode V) and a subradiant mode (Figure 2a,b-3, blue curves, mode VI). The electric-field magnitude distribution and direction (Figure 2c,d, V and VI) clearly show the two types of coupling between the ring and the disk, which is comparable to previous studies.[29] Actually the antibonding mode V and bonding mode VI can also be excited when the polarization is parallel to the split gap. The dipole of the split ring can be present, though the symmetry is broken in this polarization configuration.[43,44] The simulated electric field distribution of SRR/D at 945 nm (a dip in Figure 2b-3) shows that the antibonding mode is formed when the polarization is parallel to the split gap (Supporting Information, S5). When the electric field is parallel to the split gap, the high-order narrow magnetic modes of SRR (Figure 2b-2, red curve, mode III and IV) are spectrally overlapped with a broader super-radiant coupled electric dipole mode of SRR/D (Figure 2b-3, blue curve, mode V), resulting in significant Fano resonance spectrally. After this Fano coupling, the dips III and IV (Figure 2b-2, red line) will be presented as the peaks VII and VIII (Figure 2b-3, red line),

respectively, within the broad antibonding mode V. As Figure 2b-3 shows, a small extraordinary transmission peak arising at 764 nm corresponds to the Fano interaction between octupole magnetic mode of SRR (mode IV) and coupled dipole mode of SRR/D (mode V). Experimentally, the transmission peak at 916 nm (indicated by black arrow) inside another broad peak ~834 nm are corresponding to the Fano resonance between the two modes (Figure 2a-3, red-curve). The quadrupole magnetic mode of the SRR (~ 1060 nm, Figure 2a-2, red curve) has a larger absorption cross section than the octupole mode (~ 871 nm, Figure 2a-2, red curve), but the energy overlapping with the super-radiant SRR/D mode is smaller (Figure 2a-3). Therefore, the depth of Fano resonance involved quadrupole is not as high as that of octupole. The Fano coupling effect between the high-order magnetic modes of SRR and the super-radiant mode of SRR/D can be supported by surface electric-field magnitude distribution and electric field direction in Figure 2c,d, mode VII and VIII.

The wavelength and line shape of the surface plasmon resonance in SRR/D nanocavity as well as the Fano resonance coupling can be tuned over a wide range through varying the dimensions of the SRR and disk. Figure 3 shows measured (a) and simulated (b) transmission spectra of SRRs with varied split angle of 30°, 60°, 90°, 120°. The SEM images are displayed in Figure 3c for each corresponding angle. The electric field is set to be parallel to the split gap, to explore the interaction between magnetic and electric modes. In U-shaped SRR, it is well demonstrated that the magnetic mode frequency is proportional to $(LC)^{-1/2}$,[45] where L is the inductance of SRR, C is the capacitance between the two arms and inversely proportional to gap distance.[46] As the increasing of split angle, the octupole and quadrupole modes of the SRR are blue-shifted because of the decrease of capacitance between the two tips of the SRR. The increase of split angle from 30° to 120° leads to resonance blue-shifts of quadrupole (indicated by black arrows, Figure 3a) and octupole magnetic modes (indicated by green arrows, Figure 3a) of 150 and 100 nm, respectively. The measured resonance position variations are in good agreement with simulations. Additionally, the depth of Fano-interference spectra features is tuned. The larger the gap is, the weaker capacitive coupling between two arms of the SRRs, leading to a lower resonance absorption cross section.[5] For instance, as the split angle is increased to be 120°, octupole magnetic mode of SRRs is hard to be resolved. In SRR/D, the depth and position of Fano resonances are tuned correspondingly with the shifts of SRR's fundamental resonance modes, as shown in Figure 3d,e. Both of the quadrupole (indicated by black arrows, Figure 3d) and octupole (indicated by green arrows, Figure 3d) magnetic modes involved Fano resonance blue-shift as the split gap increases. With the decreasing spectra overlapping between SRR's octupole

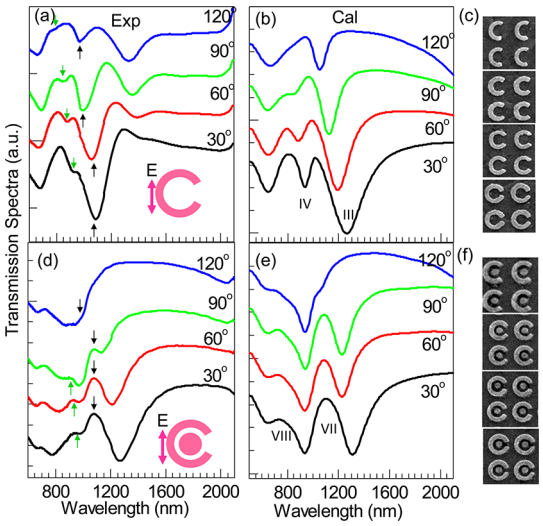

Figure 3. (a–c) Experimental (a) and calculated (b) transmission spectra, and SEM images (c) of SRR with differenct split angle. (d–f) Experimental (d) and calculated (e) transmission spectra, and SEM images (f) of SRR/D with different split angle. The dimensions are R_1= 200 nm, R_2 = 110 nm, R_3 = 75 nm. The split angle is varied from 30°, 60°, 90°, to 120°. The incidence electric field is indicated in (a) and (d).

magnetic mode and SRR/D's radiant dipole mode, the corresponding Fano resonance induced extraordinary transmission peak becomes weaker and nearly disappears when the split angle is 120°. Although the spectra overlapping between octupole magnetic mode and the dipole mode is higher with a larger split gap, the Fano resonance becomes less pronounced because of the significantly compressed resonance absorption cross section of the magnetic mode. As a contrast, larger overlapping between quadrupole magnetic mode of SRR and the super-radiant mode of SRR/D is obtained as the increasing of split gap, and accordingly the Fano resonance feature with asymmetric peaks arises (90°).

In full ring/disk nanocavities and planar nanoclusters, plasmonic modes and thus Fano resonance are highly dependent on the interparticle gap. A stronger coupling can be obtained at a shorter distance, leading to larger plasmonic mode separations or shifts. Here the inner disk diameter is varied to tune the plasmon modes and their coupling. Figure 4a,b shows the measured and simulated transmission spectra of SRR/D with varied radius when the electric field is parallel to the split gap. As the disk radius R_3 increases from 65 to 80 nm (R_1 = 200 nm, R_2 = 110 nm, θ = 30°), referring to a decreasing of the interparticle gap from 45 to 30 nm, the Fano resonance induced transmission in SRR/D are red-shifted from 885 to 961 nm for octupole magnetic Fano resonance (Figure 4a, green arrows indicate). The decreasing energy overlapping between the two interfered modes leads to a lower Fano resonance depth. Meanwhile the evidently asymmetric transmission dip due to quadrupole magnetic resonance becomes symmetric as the magnetic mode moves out of the interference frequency regime (black arrows indicate).

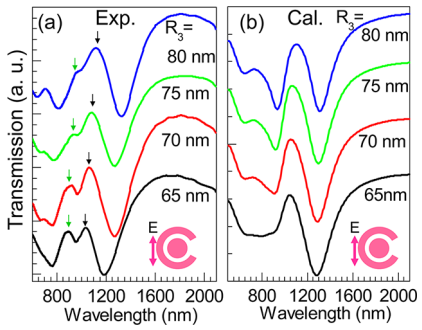

Figure 4. Transmission spectra of SRR/disk varied with inner disk size. The inner disk radius is indicated along with each curve. (a) Measured transmission spectra. (b) Simulated transmission spectra.

The SRR/D Fano resonances show high sensitivity in response to a local effective refractive index change, suggesting potential applications in chemical and biological sensing. Recently, the capabilities of U-shaped metamaterials on refractive index sensing and surface-enhanced Raman spectroscopy have been well-established.[37−39] In addition, Fano-resonance-based sensing with high sensitivity and figure of merit (FOM) has been demonstrated.[47−49] To evaluate the refractive index sensitivity in optical frequency regime, we measured the transmission spectra of SRR/D devices with solutions of different refractive index. Glycerol, widely used in pharmaceutical formulations, is selected for its low melting temperature of ∼18 °C and refractive index of 1.4746. The glycerol solution was dissolved in distilled water at room temperature. The refractive index of the mixed solution is decided by the glycerol concentration, such as graded glycerol concentration of 10, 28, 44, and 64% gives refractive index of 1.3448, 1.3676, 1.3897, and 1.4189, respectively. The glycerol/water solution was drop-casted on the chip surface, and a coverslip glass was put on to make sure the patterns are contacted fully and uniformly. After the measurement, the same chip was soaked in the distilled water and then carefully cleaned with a heavy rinse of distilled water. This cleaning method was proven to be effective by retaking the transmission spectra, which gave identical spectra obtained from the same sample before applying glycerol. The measured transmission spectra of SRR/D in different solutions are presented in Figure 5a. SRR/D with dimension of $R_1 = 200$ nm, $R_2 = 110$ nm, $R_3 = 70$ nm and θ = 30° is chosen for sensing for its relatively significant Fano features suggested by the above studies. With the increasing of glycerol concentration, the resonance peaks red-shifted, as shown in Figure 5a. The Fano resonances are more pronounced as the refractive index is ∼1.3−1.4 because of the increase of spectral overlapping between SRR magnetic and disk dipole modes. The Fano resonance involved quadrupole magnetic mode, indicated by arrows in Figure 5a, is extracted out and plotted as a function of

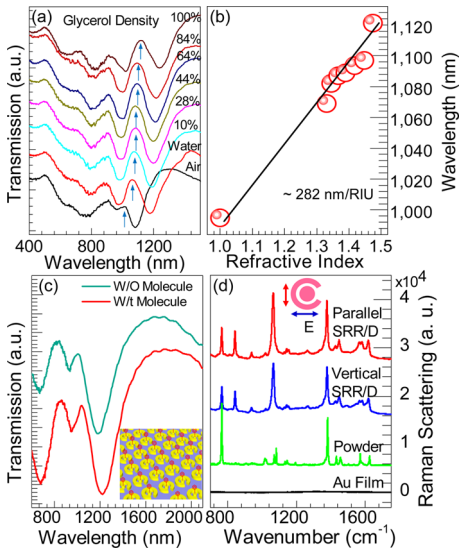

Figure 5. Refractive index sensing and surface enhanced Raman scattering of SRR/D arrays. (a) Measured transmission spectra of SRR/D in glycerol/water with different concentration. (b) Resonance frequency of SRR/D extracted from (a) as a function of refractive index. (c) Transmission spectra evolution of SRR/D array before and after attachment of monolayer 2-naphthalenethiol molecules. Inset: Schematic of monolayer 2-naphthalenethiol on SRR/D array. (d). Surface enhanced Raman scattering of 2-naphthalenethiol in two polarizations.

environment refractive index. As displayed in Figure 5b, the refractive index dependence of Fano resonance frequency can be well fitted by a linear equation, demonstrating the sensitivity up to ∼282 nm/RIU. The figure of merit, FOM = $\delta\lambda/\lambda_{FWHM}$, is evaluated to be 4, where $\delta\lambda$ is the refractive index sensitivity for a special mode, and λ_{FWHM} is the full-width at half-maximum of the mode. Previous double split-ring resonators fabricated by hole-mask method has achieved the sensitivity of 520 nm/RIU and the FOM of 2.9; the plasmonic oligomers fabricated by angle-controlled colloidal nanolithography have the sensitivity of 530 nm/RIU and the FOM of 17.[47,48] The highest FOM of EBL fabricated structures can be up to 5.7.[27] Our FOM result is comparable in the EBL fabricated structures, and the sensitivity could be further improved by optimizing the size, gap angle and the coupling distance.

It should be noted that the Glycerol and water molecules serve a different dielectric surrounding, exhibiting no specific chemical bonding. Here we further demonstrate that the SRR/D is promising in surface chemical sensing based on Fano resonance response. A monolayer of 2-naphthalenethiol molecules are bounded to Au SRR/D surface by utilizing the thiol group-Au bonding (Figure 5c, inset). The quadrupole-related magnetic Fano resonance mode exhibits red-shift of 32 nm (Figure 5c). The SRR/D also shows its potential in surface-enhanced Raman scattering. Figure 5d shows the Raman spectra of 2-naphthalenethiol on SRR/D with two polarization configurations as indicated inset; powder and molecules bond to Au film,

from top to bottom, respectively. The excitation laser wavelength is 785 nm. In order to exclude the chemical enhancement, Raman peak around 1379.4 cm^{-1} due to ring−ring stretching has been chosen to understand the Raman signal enhanced by surface plasmon. The SERS enhancement factor EF_{SERS}, evaluated by

$$EF_{SERS} = \frac{I_{SERS} \times N_{bulk}}{I_{bulk} \times N_{SERS}}$$

can be as high as 1.2×10^6 for the parallel polarization, where I_{bulk} and I_{SERS} are Raman intensity from powder and monolayer molecules on SRR/D surface, respectively, and N_{bulk} and N_{SERS} are excited numbers of molecules in powder and on SRR/D surface, respectively.

CONCLUSION

In summary, plasmonic coupling in high-quality SRR/disk structures is investigated. The quadrupole and octupole magnetic modes are coupled with super-radiant SRR/D modes, leading to two Fano asymmetric resonance features spectrally. As the increasing of split angle and interparticle separation, the Fano resonances are blue-shifted as well as the smaller depth of Fano resonances due to the decreased capacitive coupling. The refractive index sensing of Fano resonance is ~282 nm/RIU. The result will be important not only for understanding the interference of magnetic and electric high order modes coupled with electric dipole modes, but also for developing a number of plasmon-based photonic devices.

METHODS

Electron Beam Lithography Methods. A layer of commercial electron beam resist poly(methyl methacrylate) (PMMA, 950 A4, Microchem, USA) was spin-coated onto the ITO glass and then baked at 180 °C for 18 min. A JEOL 7001F scanning electron microscope (SEM) equipped with a nanometer pattern generation system (NPGS) was used to pattern the arrays. The exposed substrate was developed in methyl isobutyl ketone (MIBK), isopropyl alcohol (IPA) solution (1:3), followed by a deposition of 30 nm Au film with 2 nm Cr as adhesion layer using thermal evaporator (Elite Engineering, Singapore) and a standard liftoff process in acetone.

Optical Characterization. The transmission spectra are measured by a commercial transmission/reflectance microspectrometer (Craic 20/20). The linearly polarized white light from a Xe lamp is focused onto the sample normally from bottom. The transmitted light is collected by a reflective objective (36×, numerical aperture: 0.4) and spectrally analyzed by a monochromator. An aperture is used to acquire transmission light from an area of ~15 μm × 15 μm, which is chosen to ensure adequate transmission flux and multiple measurements over the whole patterns. A polarizer is placed between the light source and sample to obtain the polarization-dependent spectra. The scattering spectra of individual structures are measured by a dark-field confocal spectrometer in the spectra range of 500−900 nm. A polarizer is placed between the sample and detector to conduct the polarization-dependent scattering spectra.

Conflict of Interest: The authors declare no competing financial interest.

Acknowledgment. The author Q.X. is thankful for the strong support from Singapore National Research Foundation through a Fellowship Grant (NRF-RF2009-06) and a Competitive Research Program (NRF-CRP-6-2010-2), Singapore Ministry of Education *via* two Tier2 grants (MOE2011-T2-2-051 and MOE2011-T2-2-085). He also acknowledges very strong support from Nanyang Technological University *via* start-up grant (M58110061) and New Initiative Fund (M58110100).

Supporting Information Available: Transmission spectra of SRR arrays with different period (Figure S1); scattering spectra of SRR, disk and SRR/D (Figure S2); transmission spectra dependent on disk size (Figure S3); electric field distributions of high-order magnetic modes in SRR and SRR/D (Figure S4); and dipole mode of SRR/D (Figure S5). This material is available free of charge *via* the Internet at http://pubs.acs.org.

REFERENCES AND NOTES

1. Lal, S.; Link, S.; Halas, N. J. Nano-Optics from Sensing to Waveguiding. *Nat. Photonics* **2007**, *1*, 641–648.
2. Schuller, J. A.; Barnard, E. S.; Cai, W.; Jun, Y. C.; White, J. S.; Brongersma, M. L. Plasmonics for Extreme Light Concentration and Manipulation. *Nat. Mater.* **2010**, *9*, 193–204.
3. Noginov, M. A.; Zhu, G.; Belgrave, A. M.; Bakker, R.; Shalaev, V. M.; Narimanov, E. E.; Stout, S.; Herz, E.; Suteewong, T.; Wiesner, U. Demonstration of a Spaser-Based Nanolaser. *Nature* **2009**, *460*, 1110–1112.
4. Brolo, A. G. Plasmonics for Future Biosensors. *Nat. Photonics* **2012**, *6*, 709–713.
5. Berkovitch, N.; Ginzburg, P.; Orenstein, M. Nano-Plasmonic Antennas in the Near Infrared Regime. *J. Phys.: Condens. Matter* **2012**, *24*, 073202.
6. Peng, B.; Li, G.; Li, D.; Dodson, S.; Zhang, Q.; Zhang, J.; Lee, Y. H.; Demir, H. V.; Yi Ling, X.; Xiong, Q. Vertically Aligned Gold Nanorod Monolayer on Arbitrary Substrates: Self-Assembly and Femtomolar Detection of Food Contaminants. *ACS Nano* **2013**, *7*, 5993–6000.
7. Atwater, H. A.; Polman, A. Plasmonics for Improved Photovoltaic Devices. *Nat. Mater.* **2010**, *9*, 205–213.
8. Jain, P.; Huang, X.; El-Sayed, I.; El-Sayed, M. Review of Some Interesting Surface Plasmon Resonance-Enhanced Properties of Noble Metal Nanoparticles and Their Applications to Biosystems. *Plasmonics* **2007**, *2*, 107–118.
9. Kauranen, M.; Zayats, A. V. Nonlinear Plasmonics. *Nat. Photonics* **2012**, *6*, 737–748.
10. Zhang, Q.; Shan, X.-Y.; Feng, X.; Wang, C.-X.; Wang, Q.-Q.; Jia, J.-F.; Xue, Q.-K. Modulating Resonance Modes and Q Value of a CdS Nanowire Cavity by Single Ag Nanoparticles. *Nano Lett.* **2011**, *11*, 4270–4274.
11. Peng, B.; Zhang, Q.; Liu, X.; Ji, Y.; Demir, H. V.; Huan, C. H. A.; Sum, T. C.; Xiong, Q. Fluorophore-Doped Core−Multishell Spherical Plasmonic Nanocavities: Resonant Energy Transfer toward a Loss Compensation. *ACS Nano* **2012**, *6*, 6250–6259.
12. Halas, N. J.; Lal, S.; Link, S.; Chang, W.-S.; Natelson, D.; Hafner, J. H.; Nordlander, P. Plasmonic Materials: A Plethora of Plasmonics from the Laboratory for Nano photonics at Rice University. *Adv. Mater.* **2012**, *24*, 4774–4774.
13. Ye, J.; Wen, F.; Sobhani, H.; Lassiter, J. B.; Dorpe, P. V.; Nordlander, P.; Halas, N. J. Plasmonic Nanoclusters: Near Field Properties of the Fano Resonance Interrogated with SERS. *Nano Lett.* **2012**, *12*, 1660–1667.
14. Wu, C.; Khanikaev, A. B.; Adato, R.; Arju, N.; Yanik, A. A.; Altug, H.; Shvets, G. Fano-Resonant Asymmetric Metamaterials for Ultrasensitive Spectroscopy and Identification of Molecular Monolayers. *Nat. Mater.* **2012**, *11*, 69–75.
15. Fano, U. On the Absorption Spectrum of Noble Gases at the Arc Spectrum Limit. *Nuovo Cimento* **1935**, *12*, 154–161.
16. Luk'yanchuk, B.; Zheludev, N. I.; Maier, S. A.; Halas, N. J.; Nordlander, P.; Giessen, H.; Chong, C. T. The Fano Resonance in Plasmonic Nanostructures and Metamaterials. *Nat. Mater.* **2010**, *9*, 707–715.
17. Zhou, Z.-K.; Peng, X.-N.; Yang, Z.-J.; Zhang, Z.-S.; Li, M.; Su, X.-R.; Zhang, Q.; Shan, X.; Wang, Q.-Q.; Zhang, Z. Tuning Gold Nanorod-Nanoparticle Hybrids into Plasmonic Fano

Resonance for Dramatically Enhanced Light Emission and Transmission. *Nano Lett.* **2010**, *11*, 49–55.
18. Miroshnichenko, A. E.; Flach, S.; Kivshar, Y. S. Fano Resonances in Nanoscale Structures. *Rev. Mod. Phys.* **2010**, *82*, 2257–2298.
19. Svedendahl, M.; Käll, M. Fano Interference between Localized Plasmons and Interface Reflections. *ACS Nano* **2012**, *6*, 7533–7539.
20. Francescato, Y.; Giannini, V.; Maier, S. A. Plasmonic Systems Unveiled by Fano Resonances. *ACS Nano* **2012**, *6*, 1830–1838.
21. Hao, F.; Sonnefraud, Y.; Dorpe, P. V.; Maier, S. A.; Halas, N. J.; Nordlander, P. Symmetry Breaking in Plasmonic Nanocavities: Subradiant LSPR Sensing and a Tunable Fano Resonance. *Nano Lett.* **2008**, *8*, 3983–3988.
22. Woo, K. C.; Shao, L.; Chen, H.; Liang, Y.; Wang, J.; Lin, H.-Q. Universal Scaling and Fano Resonance in the Plasmon Coupling between Gold Nanorods. *ACS Nano* **2011**, *5*, 5976–5986.
23. Fan, J. A.; Bao, K.; Sun, L.; Bao, J. M.; Manoharan, V. N.; Nordlander, P.; Capasso, F. Plasmonic Mode Engineering with Templated Self-Assembled Nanoclusters. *Nano Lett.* **2012**, *12*, 5318–5324.
24. Lassiter, J. B.; Sobhani, H.; Knight, M. W.; Mielczarek, W. S.; Nordlander, P.; Halas, N. J. Designing and Deconstructing the Fano Lineshape in Plasmonic Nanoclusters. *Nano Lett.* **2011**, *12*, 1058–1062.
25. Fan, J. A.; Bao, K.; Wu, C.; Bao, J.; Bardhan, R.; Halas, N. J.; Manoharan, V. N.; Shvets, G.; Nordlander, P.; Capasso, F. Fano-Like Interference in Self-Assembled Plasmonic Quadrumer Clusters. *Nano Lett.* **2010**, *10*, 4680–4685.
26. Brown, L. V.; Sobhani, H.; Lassiter, J. B.; Nordlander, P.; Halas, N. J. Heterodimers: Plasmonic Properties of Mismatched Nanoparticle Pairs. *ACS Nano* **2010**, *4*, 819–832.
27. Lassiter, J. B.; Sobhani, H.; Fan, J. A.; Kundu, J.; Capasso, F.; Nordlander, P.; Halas, N. J. Fano Resonances in Plasmonic Nanoclusters: Geometrical and Chemical Tunability. *Nano Lett.* **2010**, *10*, 3184–3189.
28. Fang, Z.; Cai, J.; Yan, Z.; Nordlander, P.; Halas, N. J.; Zhu, X. Removing a Wedge from a Metallic Nanodisk Reveals a Fano Resonance. *Nano Lett.* **2011**, *11*, 4475–4479.
29. Sonnefraud, Y.; Verellen, N.; Sobhani, H.; Vandenbosch, G. A. E.; Moshchalkov, V. V.; Van Dorpe, P.; Nordlander, P.; Maier, S. A. Experimental Realization of Subradiant, Superradiant, and Fano Resonances in Ring/Disk Plasmonic Nanocavities. *ACS Nano* **2010**, *4*, 1664–1670.
30. Habteyes, T. G.; Dhuey, S.; Cabrini, S.; Schuck, P. J.; Leone, S. R. Theta-Shaped Plasmonic Nanostructures: Bringing "Dark" Multipole Plasmon Resonances into Action *via* Conductive Coupling. *Nano Lett.* **2011**, *11*, 1819–1825.
31. Zhang, Q.; Shan, X.-Y.; Zhou, L.; Zhan, T.-R.; Wang, C.-X.; Li, M.; Jia, J.-F.; Zi, J.; Wang, Q.-Q.; Xue, Q.-K. Scattering Focusing and Localized Surface Plasmons in a Single Ag Nanoring. *Appl. Phys. Lett.* **2010**, *97*, 261107.
32. Zhou, W.; Odom, T. W. Tunable Subradiant Lattice Plasmons by out-of-Plane Dipolar Interactions. *Nat. Nanotechnol.* **2011**, *6*, 423–427.
33. Chen, H.; Shao, L.; Ming, T.; Woo, K. C.; Man, Y. C.; Wang, J.; Lin, H.-Q. Observation of the Fano Resonance in Gold Nanorods Supported on High-Dielectric-Constant Substrates. *ACS Nano* **2011**, *5*, 6754–6763.
34. Nordlander, P. Plasmonics: The Dark Side of the Ring. *Nat. Nanotechnol.* **2013**, *8*, 76–77.
35. Shafiei, F.; Monticone, F.; Le, K. Q.; Liu, X.-X.; Hartsfield, T.; Alu, A.; Li, X. A Subwavelength Plasmonic Metamolecule Exhibiting Magnetic-Based Optical Fano Resonance. *Nat. Nanotechnol.* **2013**, *8*, 95–99.
36. Rahmani, M.; Lei, D. Y.; Giannini, V.; Lukiyanchuk, B.; Ranjbar, M.; Liew, T. Y. F.; Hong, M.; Maier, S. A. Subgroup Decomposition of Plasmonic Resonances in Hybrid Oligomers: Modeling the Resonance Lineshape. *Nano Lett.* **2012**, *12*, 2101–2106.
37. Xu, X.; Peng, B.; Li, D.; Zhang, J.; Wong, L. M.; Zhang, Q.; Wang, S.; Xiong, Q. Flexible Visible–Infrared Metamaterials and Their Applications in Highly Sensitive Chemical and Biological Sensing. *Nano Lett.* **2011**, *11*, 3232–3238.
38. Zhang, J.; Cao, C.; Xu, X.; Liow, C.; Li, S.; Tan, P.-H.; Xiong, Q. Tailoring Plasmonic Metamaterials for DNA Molecular Logic Gate, **2013**, Submitted.
39. Cao, C.; Zhang, J.; Wen, X.; Dodson, S. L.; Dao, N. T.; Wong, L. M.; Wang, S.; Li, S.; Phan, A. T.; Xiong, Q. Metamaterials-Based Label-Free Nanosensor for Conformation and Affinity Biosensing. *ACS Nano* **2013**, *7*, 7583–7591.
40. Enkrich, C.; Wegener, M.; Linden, S.; Burger, S.; Zschiedrich, L.; Schmidt, F.; Zhou, J.; Koschny, T.; Soukoulis, C. Magnetic Metamaterials at Telecommunication and Visible Frequencies. *Phys. Rev. Lett.* **2005**, *95*, 203901.
41. Fu, Y. H.; Zhang, J. B.; Yu, Y. F.; Luk'yanchuk, B. Generating and Manipulating Higher Order Fano Resonances in Dual-Disk Ring Plasmonic Nanostructures. *ACS Nano* **2012**, *6*, 5130–5137.
42. Johnson, P. B.; Christy, R. W. Optical Constants of the Noble Metals. *Phys. Rev. B: Solid State* **1972**, *6*, 4370–4379.
43. Liu, S. D.; Yang, Z.; Liu, R. P.; Li, X. Y. Plasmonic-Induced Optical Transparency in the Near-Infrared and Visible Range with Double Split Nanoring Cavity. *Opt. Express* **2011**, *19*, 15363–15370.
44. Liu, S. D.; Yang, Z.; Liu, R. P.; Li, X. Y. Multiple Fano Resonances in Plasmonic Heptamer Clusters Composed of Split Nanorings. *ACS Nano* **2012**, *6*, 6260–6271.
45. Linden, S.; Enkrich, C.; Wegener, M.; Zhou, J. F.; Koschny, T.; Soukoulis, C. M. Magnetic Response of Metamaterials at 100 Terahertz. *Science* **2004**, *306*, 1351–1353.
46. Gorkunov, M.; Lapine, M.; Shamonina, E.; Ringhofer, K. H. Effective Magnetic Properties of a Composite Material with Circular Conductive Elements. *Eur. Phys. J. B* **2002**, *28*, 263–269.
47. Zhao, J.; Frank, B.; Burger, S.; Giessen, H. Large-Area High-Quality Plasmonic Oligomers Fabricated by Angle-Controlled Colloidal Nanolithography. *ACS Nano* **2011**, *5*, 9009–9016.
48. Zhao, J.; Zhang, C. J.; Braun, P. V.; Giessen, H. Large-Area Low-Cost Plasmonic Nanostructures in the NIR for Fano Resonant Sensing. *Adv. Mater.* **2012**, *24*, Op247–Op252.
49. Liu, N.; Weiss, T.; Mesch, M.; Langguth, L.; Eigenthaler, U.; Hirscher, M.; Sonnichsen, C.; Giessen, H. Planar Metamaterial Analogue of Electromagnetically Induced Transparency for Plasmonic Sensing. *Nano Lett.* **2010**, *10*, 1103–1107.